Renewable Energy 133 (2019) 663–675

Contents lists available at ScienceDirect

Renewable Energy

journal homepage: www.elsevier.com/locate/renene

An experimental study on the aerodynamic performance degradation of a wind turbine blade model induced by ice accretion process

Linyue Gao [a], Yang Liu [a], Wenwu Zhou [a, b], Hui Hu [a, *]

[a] Department of Aerospace Engineering, Iowa State University, Ames, IA 50011-2271, United States
[b] Department of Mechanical Engineering, Shanghai Jiao Tong University, Shanghai, China

ARTICLE INFO

Article history:
Received 25 April 2018
Received in revised form
30 September 2018
Accepted 7 October 2018
Available online 11 October 2018

Keywords:
Wind turbine icing
Aerodynamic performance characteristic of turbine blade
Turbine performance degradation induced by ice accretion
Unsteady force measurement
Particle image velocimetry measurement

ABSTRACT

An experimental study was conducted to characterize aerodynamic performance degradation of wind turbine blades induced by dynamic ice accretion process. The experimental study was performed in an Icing Research Tunnel with a turbine blade model under a typical glaze icing condition. Ice structures were found to accrete rapidly over both the upper and lower surfaces of the blade model after starting the ice accretion experiment. Irregular-shaped ice structures were found to disturb the airflow around the blade model greatly, resulting in large-scale flow separations and shedding of unsteady vortex structures from the ice accreting surface. The aerodynamic performance of the blade model was found to degrade significantly. The performance degradation induced by the ice accretion was found to be a strong function of the angle of attack of the blade model with more significant degradations at lower angles of attack. For the test case at the angle of attack of 5.0°, while the lift decreases to only ~12% of its original value after 600 s of the ice accretion experiment, the drag was found to increase 4.5 times correspondingly. The detailed flow field measurements were correlated with the aerodynamic force data to elucidate the underlying physics.

1. Introduction

Wind energy is one of the most promising renewable energy sources for massive production of electricity. U.S. Department of Energy has challenged the nation to produce 20% of its total power from wind by 2030. While the national average rate is only about 5.5% in 2016, Iowa is leading the nation in wind power generation with 36.6% of the state's total electricity from wind energy. While windy winter is the best season for wind energy harvest in the northern states like North Dakota, South Dakota, Minnesota and Iowa, wind turbine icing represents the most significant threat to the integrity of wind turbines in cold weathers. It has been found that ice accretion on turbine blades would decrease power production of the wind turbines significantly [1]. Ice accretion and irregular shedding during wind turbine operation would lead to load imbalances as well as excessive turbine vibrations, often causing the wind turbine to shut off [2]. Icing can also affect the tower structures by increasing stresses. This can lead to structural failures, especially when coupled to strong wind loads [3]. Icing was also found to affect the reliability of anemometers, thereby, leading to inaccurate wind speed measurements and resulting in resource estimation errors [4]. Icing issues can also directly impact personnel safety due to falling and projected large ice chunks [5]. In severe icing events, wind turbines would have to be shut down for days or months to guarantee their safety and integrity [6]. The loss of annual energy production (AEP) due to icing was found to be in the range of 20%–50% at harsh sites [7].

It is well known that, ice accretion on wind turbines can be either rime or glaze, depending on the ambient air temperatures, airflow velocities, liquid water content (LWC) levels, and median volumetric diameters (MVD) of the water droplets. In a dry regime, all the water collected in the impingement area freezes immediately to form rime ice. For a wet regime, only a fraction of the collected water freezes in the impingement area to form glaze ice and the remaining water runs back and can freeze outside the impingement area [8,9]. Usually, formation of rime ice is associated with colder temperatures, below −10 °C, lower liquid water contents, and smaller median volumetric diameters of the water droplets. Early rime ice accretion usually closely follows the original contour of the airfoil profiles due to the almost instantaneous freezing of the impinging water droplets; therefore, the

* Corresponding author.
E-mail address: huhui@iastate.edu (H. Hu).

https://doi.org/10.1016/j.renene.2018.10.032
0960-1481/

aerodynamic performance penalties due to rime ice are not as severe as those of glaze ice. Formation of glaze ice is associated with warmer temperatures, above −10 °C, higher liquid water contents, and larger median volumetric diameters [10]. Glaze is the most dangerous type of ice. Because of its wet nature, glaze ice form much more complicated shapes which are difficult to accurately predict, and the resulting ice shapes tend to substantially deform the accreting surface with the formation of "horns" and larger "feathers" growing outward into the airflow [6,11,12]. Glaze ice formation will severely decrease the airfoil aerodynamic performance by causing large scale flow separation which produces dramatic increases in drag and decreases in lift [13], which can cause a dramatic reduction in the power generation of wind turbines.

While several anti-/de-icing systems have been developed for wind turbine icing mitigation, almost all the current anti-/de-icing strategies were originally designed for aircraft anti-/de-icing applications. Many special issues related to wind turbine icing phenomena have not been properly considered in adopting those aircraft-orientated anti-/de-icing techniques for wind turbine icing mitigation. For example, the optimized airfoil shapes used to design wind turbine blades usually have much greater airfoil thickness and blunter leading edge than those used to design aircraft wings. The significant differences in the airfoil profile shapes, especially in the regions near the airfoil leading edges, are expected to greatly affect the flying trajectories and subsequent impingement of supercooled water droplets carried by the incoming airflow, thereby, change the ice accretion process over the airfoil surfaces significantly. Furthermore, polymer-composite-based turbine blades have very different surface properties (e.g., thermal conductivity) in comparison with those of metal-based aircraft wings. The effects of the significant difference in the thermal conductivity between the metal-based aircraft-wings (i.e., >200 W/mK) and the polymer-composite-based wind turbine blades (i.e., <0.5–1.0 W/mK) on the ice formation and accretion processes have not been fully explored. In addition, wind turbines operate much closer to the sea level than airplanes, thereby, are more prone to encounter with freezing rain and other low altitude, high liquid-water-content environments (such as ocean spray). Therefore, it is highly desirable to develop innovative, effective anti-/de-icing strategies tailored for wind turbine icing mitigation to ensure safer and more efficient operation of wind turbines in atmospheric icing conditions. Doing so requires a keen understanding of the underlying physics pertinent to wind turbine icing phenomena, both for the ice accretion process itself as well as for the resultant aerodynamic performance degradation of the ice accreting turbine blades.

In the present study, a comprehensive experimental investigation was conducted to investigate the dynamic ice accreting process over the surfaces of typical wind turbine blades and quantify the resultant aerodynamic performance degradation of the turbine blades during the dynamic ice accreting process. The experiment study was performed in an Icing Research Tunnel available at Iowa State University (i.e., ISU-IRT) under a typical glaze ice accretion condition. A polymer-composite-based turbine blade section model with most-commonly-used DU91-W2-250 airfoil profile in the cross section was manufactured and used for the ice accretion experiment under a typical glaze icing condition. The effects of the angle of attack (i.e., AoA) of the test model related to the incoming airflow and the airborne super-cooled water droplets on the dynamic ice accretion process and the resultant aerodynamic performance degradation characteristics were examined during the ice accretion process. While a high-speed imaging system was used to record the dynamic ice accretion process over the surfaces of the turbine blade model, the unsteady aerodynamic forces (i.e., both lift and drag) acting on the ice accreting airfoil model were measured by using two sets of high-sensitive force/moment measurement systems mounted at two ends of the test model. A high-resolution Particle Image Velocimetry (PIV) system was also synchronized with the aerodynamic force measurements to characterize the behaviors of the turbulent airflows over the ice accreting airfoil model. The detailed PIV flow field measurements were correlated with the dynamic aerodynamic force data to gain further insight into the underlying physics for a better understanding about the effects of ice accretion process on the performance of the wind turbines when operating in cold weathers. It should be noted that, while several previous studies have been carried out recently to simulate ice accretion on turbine blades through icing wind tunnel testing [14] or using "artificial" iced profiles with various types and amounts of ice accretion to investigate the aerodynamic performance of iced blades [3,5,15], the experimental work presented here is believed to be the first to examine the dynamic ice accretion process over the surface of a polymer-composite-based turbine blade model and to characterize the resultant aerodynamic performance degradations of the turbine blade model in the course of the ice accreting process.

2. Experimental setup and test model

2.1. Icing research tunnel

The ice accretion experiments were performed in an Icing Research Tunnel available at Iowa State University (i.e., ISU-IRT). As shown schematically in Fig. 1, ISU-IRT is a research-grade multi-functional icing tunnel with a transparent test section of 0.40 m × 0.40 m × 2.0 m in size. An axial fan was used to drive the airflow cycling inside the tunnel with the wind speed in the test section up to 60 m/s. The tunnel is refrigerated via a heat exchanger, which is chilled by a 30-kW compressor (Vilter™). The airflow inside ISU-IRT can be cooled down to −25 °C. An array of 8 pneumatic atomizing spray nozzles (Spraying Systems Co., 1/8 NPT-SU11) along with pressure regulators were installed at the entrance of the contraction section of ISU-IRT to inject micro-sized water droplets (i.e., MVD = ~20 μm) into the airflow. The flow rate of the water injected into the tunnel was measured directly by using a digital flow meter (Omega, FLR-1605A). By manipulating the pressure regulators on the air and water supply pipelines of the spray nozzles, the mass flow rate of the water injected into ISU-IRT,

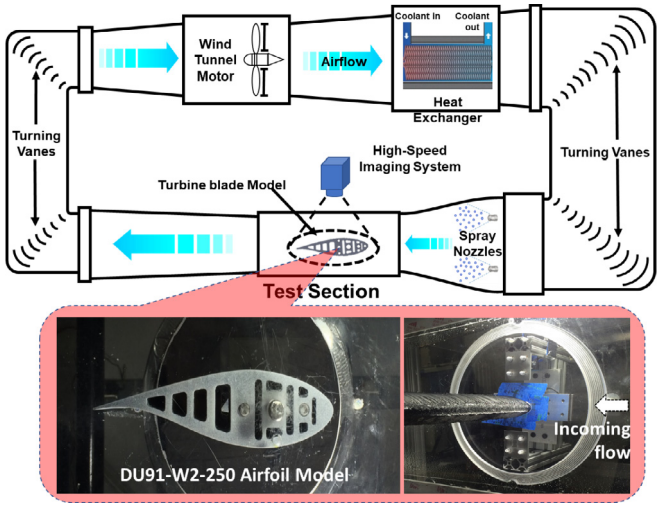

Fig. 1. Schematic of ISU-IRT and the turbine blade model used in the present study.

thereby, the liquid water content (LWC) of the airflow inside the tunnel, can be adjusted. In summary, ISU-IRT can be operated over a range of test conditions, i.e., from very dry rime ice (e.g., LWC ≈ 0.1 g/m^3) to extremely wet glaze ice (LWC > 5.0 g/m^3), to duplicate/simulate atmospheric icing phenomena over a wide range of icing conditions [8,9,16–20]. Further information about the technical parameters of ISU-IRT is available at http://www.aere.iastate.edu/icing/ISU-IRT.html.

2.2. Turbine blade model

In the present study, a widely-used, wind turbine dedicated airfoil profile, DU91-W2-250, was selected to make a wind turbine blade section model for the ice accretion experiments. As shown schematically in Fig. 1, the DU91-W2-250 airfoil, which is a cambered airfoil with a blunt trailing edge and a maximum thickness of 25% chord length, is known for its favorable aerodynamic performance and strong structural strength for wind turbine applications. DU91-W2-250 airfoil profile has been commonly used as in-board, mid-span and out-board airfoil geometry for wind turbines of various scales [21,22].

Since modern wind turbine blades are mainly made of polymer-composite materials, a polymer-composite-based DU91-W2-250 airfoil model was manufactured by using a rapid prototyping machine (i.e., 3D printer) for the ice accretion experiments of the present study. The surface of 3-D printed airfoil model was coated with several layers of spray-on primer, and then wet-sanded by using fine sandpapers (i.e., up to 2000 grit) to achieve a very smooth, glossy finish with about 25 μm in the characteristic roughness over the surface. Finally, a readily available all-weather protective spray-on enamel (Rustoleum™, Flat Protective Enamel, black in color) was coated onto the sanded surface. Supported by a stainless-steel rod, the test model was mounted at its quarter-chord and oriented horizontally in the middle of ISU-IRT test section, as shown in Fig. 1. The angle of attack (AoA) of the DU91-W2-250 airfoil model was adjustable by pivoting the test model about the supporting rod and fixing it at the desired angles as measured with a digital inclinometer.

2.3. Controlling parameters of the test cases

As described above, in comparison to rime ice accretion, glaze ice accreted over the surfaces of wind turbine blades has been found to be more problematic and could degrade the aerodynamic performance of the turbine blades more significantly, thereby, resulting in a more dramatic reduction in the power generation of the wind turbines [13]. Therefore, a typical glaze ice accretion scenario was selected in the present study in characterizing the aerodynamic performance degradation of the wind turbine blades under more severe icing conditions. More specifically, the controlling parameters in the ISU-IRT were set as the incoming airflow velocity of $V_\infty = 40.0$ m/s; airflow temperature of $T_\infty = -5.0\,^\circ$C; and liquid water content (LWC) level of LWC = 1.1 g/m^3. The corresponding chord Reynolds number of the turbine blade model is approximately 4.2×10^5 under such test conditions.

In the present study, the effects of ice accretion were examined by comparing the measured aerodynamic performance of the turbine blade model in two different situations, i.e., 1) the "clean" test case without any ice accretion over the surface of the test model as the comparison baseline; and 2) "icing" test case with ice being accreted over the surface of the test model during the ice accretion process. Table 1 summarizes the controlling parameters of the ice accretion experiment of the present study. During the experiments, the angle of attack (i.e., AoA) of the test model was changed at AoA = 5°, 10° and 15° to represent three typical operational conditions of the wind turbine blade model, i.e., the maximum lift-to-drag-ratio condition, the maximum lift condition, and a typical post-stall condition, respectively. Based on the work described in Kiefer et al. [23], Harper [24] and Nilanjan [25], the statistics of the ice accretion process and corresponding flow field characteristics over the turbine blade model are expected to be mainly two-dimensional with the experimental settings of the present study.

Table 1
The test cases of the present study.

Case No.	State	AoA [°]	LWC [g/m^3]	T_∞ [°C]	V_∞ [m/s]
1	Clean	5	–	−5.0	40.0
2	Clean	10	–	−5.0	40.0
3	Clean	15	–	−5.0	40.0
4	Icing	5	1.1	−5.0	40.0
5	Icing	10	1.1	−5.0	40.0
6	Icing	15	1.1	−5.0	40.0

2.4. Measurement systems used for the ice accretion experiments

As shown schematically in Fig. 1, a high-resolution imaging system (i.e., PCO Tech, Dimax Camera, 2 K pixels × 2 K pixels in resolution) along with a 60 mm Macro-lens (Nikon, 60 mm Nikkor 2.8D) was used in the present study to record the dynamic ice accreting process over the surface of the turbine blade model. The camera was positioned normal to the airfoil chord of the test model. Low-flicker illumination was provided by a pair of 150 W fiber-coupled halogen lamps (AmScope, HL250-AS).

In addition to acquiring the ice accretion images, two sets of high-sensitive, multi-axis force-moment transducers (i.e., ATI-IA Mini 45) were mounted at two ends of the turbine blade model to measure the unsteady aerodynamic loads (i.e., lift and drag) acting on the test model during the dynamic ice accreting process. The force/moment transducers are composed of foil strain gage bridges, which can measure the forces on three orthogonal axes, and the moment (torque) about each axis. The precision of the force-moment transducers for force measurements is ±0.25% of the full range (40 N). During the experiments, the force/torque transducers were synchronized via a 16-bit data acquisition system (NI USB-6218) for the data acquisition up to 1000 Hz. The measurement results of the force/moment transducers were used to determine the aerodynamic performance of the turbine blade model in the terms of the lift and drag coefficients (i.e., C_L and C_D), which are defined as $C_L = F_L / \left(\frac{1}{2}\rho_a V_\infty^2 S\right)$ and $C_D = F_D / \left(\frac{1}{2}\rho_a V_\infty^2 S\right)$, where, F_L and F_D are the lift and drag forces acting on the test model, ρ is the density of air, V_∞ is the velocity of the incoming airflow, S is the relevant surface area of the test model (i.e., $S = C \cdot L$ with C being the chord length and L being the spanwise length of the test model), respectively. The gaps between the ends of the test model and the adjacent walls of wind tunnel were carefully controlled to be less than 0.10% of the spanwise length of the test model, which is smaller than the recommended value of 0.20% given in Nilanjan [25]. Therefore, based on the work of Nilanjan [25], the measurement uncertainty caused by the gaps between the model ends and the walls of the wind tunnel is believed to be negligible (i.e., <2%) for the present study. The effects of the model blockage, the wind tunnel walls and wake interferences on the measurement results were also calibrated by using the methods described in Pope and Harper [24].

Since the airfoil model was mounted horizontally (i.e., in parallel to the direction of the incoming airflow) in ISU-IRT during the ice accretion experiment, while the drag force, F_D, can be measured directly by adding the measured values of the horizontal components of the aerodynamic forces acting on the test model, the lift

force, F_L, would be coupled with the weight of the ice accreted over the test model to contribute to the vertical components of the dynamic forces measured by the force-moment transducers. To decouple the weight of the ice accreted on the test model from the lift force measurements, a pilot experiment was designed in the present study to quantify the weight changes of the test model due to the ice accreted as a function of the ice accretion time. For the pilot experiment, while ISU-IRT was operated under the same icing condition as the ice accretion experiment, the weight of the test model was measured every 100 s after starting the ice accretion experiment (i.e., the ISU-IRT was switched off temporarily to measure the weight of the iced airfoil model). With the relationship between the weight of the ice accreted over the test model and the ice accretion time obtained through the pilot experiment, time evolution of the lift force acting on the ice accreting airfoil model were determined by subtracting the weight of the ice accreted on the test model from the measured vertical components of the dynamic forces acting on the turbine blade model. It was found that, after 600 s of the ice accretion process, the weight of the ice accreted over the airfoil model could reach up to ~10% of the measured lift force for the test case with the test model at 10° angle of attack (i.e., AoA = 10°). Under each icing condition, the experiments were repeated multiple times (3–5 times), and the measured lift and drag coefficients obtained under the same icing conditions were compared quantitatively. It was found that, the variations of the measured lift and drag coefficients under the same icing conditions were less than ~5% and ~8%, respectively.

In the present study, a high-resolution PIV system was also used to achieve flow field measurements to quantify the turbulence airflow over the airfoil surface of the turbine blade model during the dynamic ice accreting process. Fig. 2 shows the schematic of the experimental setup used for PIV measurements. For the PIV measurements before and after the ice accretion process, the incoming airflow was seeded with ~ 1 μm oil droplets by using a smoke generator, while the airborne supercooled water droplets were used as the tracer particles for the PIV measurements during the ice accretion process. It should be noted that, since the supercooled water droplets suspended in the incoming airflow have a mean volume diameter (MVD) of ~20 μm, the corresponding Stokes number of the water droplets was estimated to be about 1.0 (i.e., $St \approx 1.0$), indicating a reasonable dynamic response of the droplets to follow the incoming airflow. The illumination of for the PIV measurements was provided by a double-pulsed Nd: YAG laser (i.e., New Wave, Gemini PIV 200) adjusted on the second harmonic and emitting two pulses of 200 mJ at the wavelength of 532 nm. A set of convex and concave cylindrical lenses along with optical mirrors were used to generate a laser sheet to illuminate the PIV tracers in the vertical plane passing through the middle span of the test model. The thickness of the laser sheet in the measurement region was set to be about 1.0 mm. A high-resolution 16-bit digital camera (2 K pixels × 2 K pixels, PCO2000, CookeCorp) was used for PIV image acquisition with the axis of the cameras perpendicular to the laser sheet. The digital camera and the double-pulsed Nd: YAG laser were connected to a workstation (host computer) via a digital delay generator (Berkeley Nucleonics, Model 565), which controlled the timing of the laser illumination and the image acquisition.

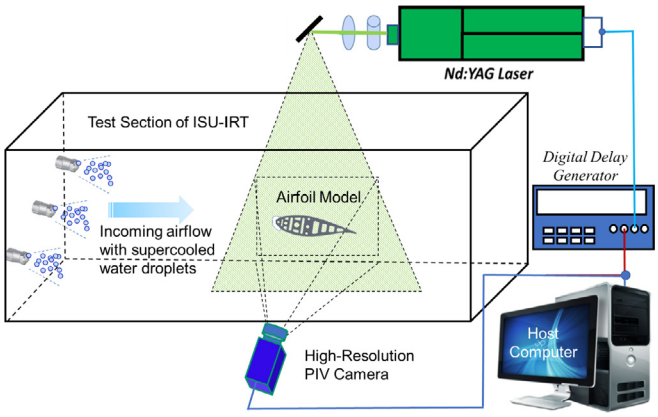

Fig. 2. Experimental setup used for the PIV measurements.

After PIV image acquisition, instantaneous PIV velocity vectors were obtained by a frame to frame cross-correlation technique involving successive frames of patterns of particle images in an interrogation window of 32 × 32 pixels. An effective overlap of 50% of the interrogation windows was employed in PIV image processing, which result in a spatial resolution of 2.0 mm × 2.0 mm for the PIV measurements. After the instantaneous velocity vectors were determined, the ensemble-averaged flow quantities were obtained from the instantaneous PIV measurements. In the present study, a cinema sequence of over 1000 frames of instantaneous PIV image pairs were obtained to ensure a good convergence of the ensemble-averaged flow statistics based on the PIV measurements. The measurement uncertainty level for the instantaneous PIV velocity measurement was estimated to be within 2.0%.

3. Measurement results and discussion

3.1. Quantification of the aerodynamic characteristics of the "clean" test model

In the present study, the aerodynamic characteristics of the "clean" turbine blade section model (i.e., without any ice accretion over the surface of the test model) were measured before performing ice accretion experiment, which is used as the baseline to evaluate the effects of the ice accretion on the aerodynamic performance degradation of the test model. Fig. 3 shows the measurement results in the terms of the lift and drag coefficients of the "clean" DU91-W2-250 airfoil model at the chord Reynolds number of $Re = 4.2 \times 10^5$. The experimental data for the same DU91-W2-250 airfoil obtained by the research team at TU Delft at a higher chord Reynolds number of $Re = 7.0 \times 10^5$ [21,22,26] are also plotted in the same graph for quantitative comparisons. It should also be noted that, while the experiments of the present study were performed in ISU-IRT with a relatively high turbulence level (i.e., approximately 3.0% in the incoming airflow due to the existence of the water spray system installed in ISU-IRT), the measurement results of TU Delft team were obtained in a much quiet wind tunnel with a much lower turbulence level (i.e., <0.1%) as described in Timmer et al. [21]. It can be seen clearly that, the two sets of measurement data for the airfoil lift coefficients agree with each other well at the angles of attack before airfoil stall, i.e., at AoA <10°. As the angle of attack increases beyond the airfoil stall angle, the two lift curves start to diverge, as shown clearly in Fig. 3. Unlike to those of the measurement results reported in Timmer et al. [21] at the higher Reynolds number of $Re = 7.0 \times 10^5$, the measured lift data of the present study reveals a much more flattened lift curve at the higher angles of attack (i.e., greater than the airfoil stall angels of AoA > 11°). Since the lower chord Reynolds number and the higher turbulence level in ISU-IRT would promise a more intense energy exchange between the high-momentum freestream flow and the boundary layer flow near the airfoil surface, it contributes to a much gentle airfoil stall, as revealed from the measured lift data given in Fig. 3. It should also be noted that, the higher turbulence level in ISU-IRT would induce intensified viscosity, thereby, a larger skin friction acting on the airfoil surface, as described in Yep et al.

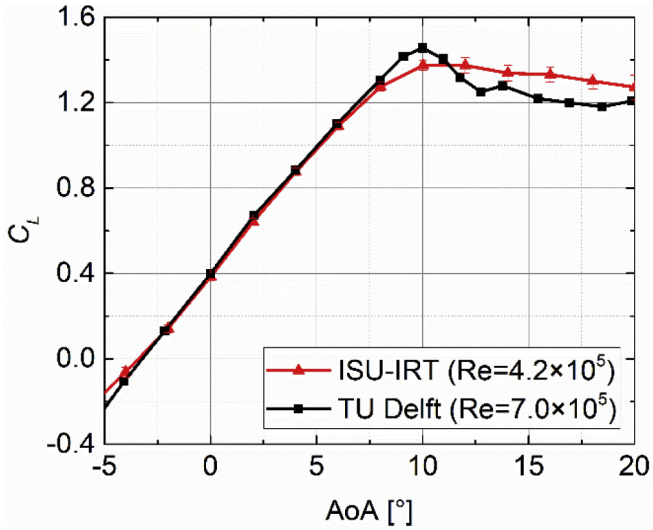

(a). Lift coefficients vs. the angle of attack

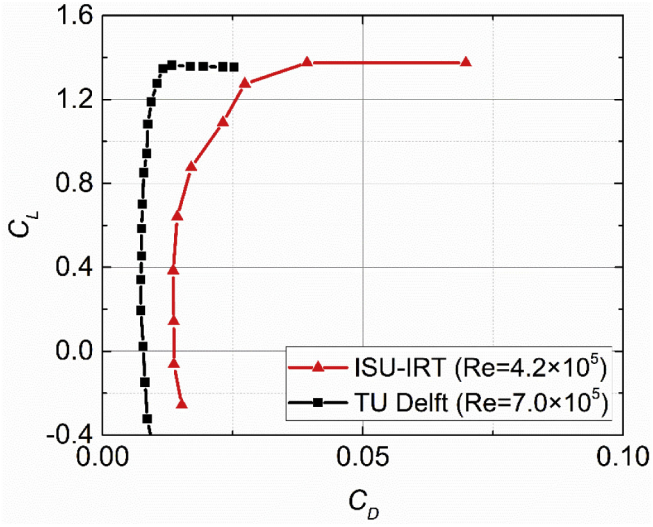

(b). Lift coefficients vs. drag coefficients

Fig. 3. The aerodynamic performance of the "clean" turbine blade model.

[27] and Wang et al. [28]. Therefore, the measured drag coefficients of the present study (i.e., ~3.0% turbulence level in the incoming airflow) were found to be slightly greater than those reported by Timmer et al. [21] with a much lower turbulence level (i.e., <0.1%) of the incoming airflow.

3.2. High-speed imaging of the dynamic ice accreting process over the test model

After measuring the aerodynamic characteristics of the "clean" turbine blade model, the refrigeration system of ISU-IRT was switched on in order to characterize the aerodynamic performance degradation of the same test model induced by the ice accretion. To perform the ice accretion experiment, ISU-IRT was operated at a pre-scribed frozen-cold temperature level (e.g., $T_\infty = -5\,^\circ$C for the present study) for at least 20 min under a dry operation condition (i.e., without turning on the water spray system) to ensure that ISU-IRT reached at a thermal steady state. After switching on the water spray system, the supper-cooled water droplets carried by the frozen-cold airflow would impinge onto the surface of the test model to start the dynamic ice accreting process.

Figs. 4 and 5 show the typical snapshots of the acquired images to reveal the dynamic ice accreting process on the both upper and lower surfaces of the turbine blade model as a function of the time after switching on the water spray system of ISU-IRT at the time instance of $t = t_0$ with the test model at AoA = 5°, 10°, and 15°, respectively. As aforementioned, under the icing test condition of the present study (i.e., $V_\infty = 40$ m/s, $T_\infty = -5\,^\circ$C, and LWC = 1.1 g/m^3), the ice accretion over the surface of the test model is expected to be of a typical glaze icing process (i.e., with obvious surface water runback process and formation of transparent ice structures), as described in the studies of Waldman and Hu [29] and Liu et al. [8].

As revealed clearly from the acquired ice accretion images given in Figs. 4 and 5, upon the impingement of the super-cooled water droplets carried by the incoming airflow, ice formation and accretion were found to occur very rapidly on both the suction side (i.e., upper surface) and pressure side (i.e., lower surface) of the test model. As expected, the ice accretion process was found to occur initially within the direct impingement zone of the super-cooled water droplets, i.e., within a narrow region near the stagnation line of the airfoil as described by Papadakis et al. [30]. Under such a rather wet icing condition used in the present study, with a large number of super-cooled water droplets impinging onto the airfoil surface, tremendous latent heat of fusion would be released associated with the rapid solidification of the impacted water mass over the airfoil surface. As described in Liu et al. [8], since the heat transfer process over the airfoil surface under such a wet icing condition would not be able to remove/dissipate all the released latent heat of fusion immediately, only a portion of the impinged water droplets would be solidified and turn into ice upon impact, while the rest of the impinged water mass would stay in liquid state, and as able to flow freely over the airfoil surface. As driven by the boundary layer airflow over the airfoil surface, the unfrozen surface water would run back along the airfoil surface to form rivulet flows, as described in Zhang et al. [18]. The rivulet flows of the runback surface water were found to be frozen into ice

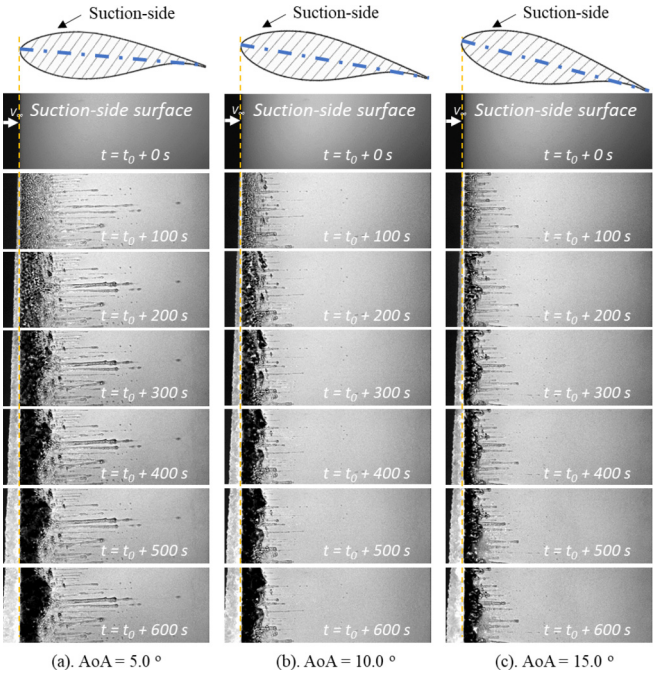

(a). AoA = 5.0 ° (b). AoA = 10.0 ° (c). AoA = 15.0 °

Fig. 4. Acquired snapshot images to reveal the dynamic ice accreting process over the suction-side surface (i.e., upper surface) of the turbine blade model.

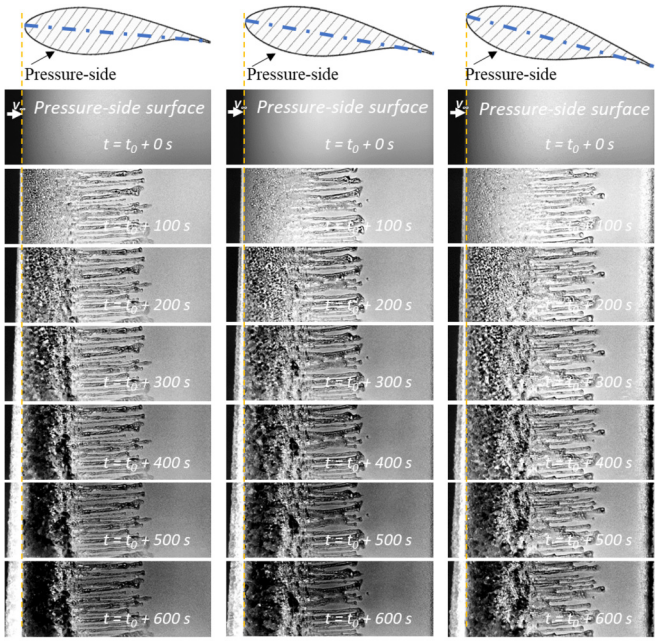

(a). AoA = 5.0° (b). AoA = 10.0° (c). AoA = 15.0°

Fig. 5. Acquired snapshot images to reveal the dynamic ice accreting process over the pressure-side surface (i.e., lower surface) of the turbine blade model.

eventually at the further downstream locations, i.e., beyond the direct impact zone of the super-cooled water droplets near the airfoil leading edge. As a result, rivulet-shaped ice structures were found to become the dominate features of the ice accretion over both the upper and lower surfaces of the turbine blade model, as shown clearly in Figs. 4 and 5.

In the present study, with the test model being mounted at AoA = 5°, 10° and 15° during the ice accretion experiment, the stagnation line on the airfoil surface would be located on the pressure side (i.e., lower surface) of the test model. Therefore, there will be much more super-cooled water droplets impinging onto the lower surface of the test model than those on the airfoil upper surface. Corresponding to the much greater amount of the water mass collected on the lower airfoil surface during the ice accretion experiment, much more rivulet-shaped ice structures were observed to accrete over the pressure side (i.e., lower surface) of the turbine blade model, in comparison with those over the suction side (i.e., upper surface) of the test model.

By comparing the test cases with the test model at different angles of attack, it can be seen clearly that, with an increasing angle of attack of the test model, while the total amount of the ice structures accreted over the suction-side surface (i.e., upper surface) of the test model were found to become less and less, more and more rivulet-shaped ice structures were found to accrete over the pressure-side surface (i.e., lower surface) of the test model. This can be explained by the fact that, as the angle of attack of the test model increases, the stagnation line over the airfoil surface would move further downstream over the lower surface of the test model (i.e., moving further away from the airfoil leading edge). As a result, more and more supper-cooled droplets would impinge directly over the airfoil lower surface, instead of the upper surface of the turbine blade model. The acquired ice accretion images given in Fig. 5 also revealed, while most of the accreted ice structures were found to concentrate near the airfoil leading edge at relatively low angles of the attack (i.e., AoA = 5° and 10°), some tiny ice features were also observed to accrete over the pressure-side of the airfoil surface near the trailing edge at comparatively larger angle of attack (e.g., AOA = 15°). This is believed to be caused by the fact that, with the test model being at relatively large angles of attack (e.g., AOA = 15°), some of the airborne, super-cooled water droplets would be able to impinge directly onto the pressure-side surface in the region near the airfoil trailing edge. Furthermore, the flow separation and the shedding of the vortex structures from the airfoil trailing edge at relatively large angles of attack (e.g., AOA = 15°) would also contribute the ice formation/accretion near the airfoil trailing edge as shown in Fig. 5(c).

It should be noted, while majority of ice accretions were found to occur over the lower surface of the test model, the irregular-shaped ice structures accreted over the upper surface of the test model would cause significant disturbances to the incoming airflow and further cause large-scale flow separation over the upper surface of the test model, resulting in tremendous degradation in the aerodynamic performance of the test model. The formation of the large-scale flow separation zone as well as generation and shedding of unsteady vortex structures induced by the ice accretion over the upper surface of the test model were visualized clearly from the PIV measurement results, as shown in the next section.

3.3. PIV measurements to quantify the airflow over the test model during the dynamic icing process

As described, a high-resolution digital PIV system was used in the present study to quantify the transient behavior of the airflow field over the surface of the test model during the dynamic icing process. Fig. 6 shows some typical instantaneous PIV measurement results to reveal the dynamic changes of the turbulent airflow over the ice accreting surface of the test model under the icing test conditions of $V_\infty = 40.0$ m/s, $T_\infty = -5.0$ °C, and LWC = 1.1 g/m^3.

As shown clearly in Fig. 6(a), before starting the ice accretion process, i.e., at time of $t = t_0 + 0$ s, the incoming airflow was found to conform well to the streamlined profile of the turbine blade model when the test model was mounted at AoA = 10° (i.e., smaller than the airfoil stall angle). Shortly after the ice accretion process starts, e.g., at the time of $t = t_0 + 25$ s, while evident ice structures were found to accrete over both upper and lower surfaces of the test model, the irregular-shaped ice structures accreted over the suction-side airfoil surface would affect the development of the boundary layer flow over the test surface significantly, resulting in the flow separation over the airfoil surface near the airfoil trailing edge, as revealed clearly in Fig. 6(b). As the time goes by, with more super-cooled water droplets impinging onto the airfoil surface, the irregular-shaped ice structures accreted over the test model were found to grow up rapidly, extruding further into the incoming airflow. As a result, the flow separation zone formed over the airfoil surface was found to expand further upstream and become bigger and bigger, as shown clearly from the PIV measurement results in Fig. 6(c) and (d). In addition to the formation of the large-scale flow separation, unsteady vortex structures were also found to be generated and shedding periodically from the ice accreting airfoil surface. With a continuous growth of the ice structures over the test model at later time of the ice accretion process, e.g., after the time of $t = t_0 + 150$ s, while generation and shedding of unsteady vortex structures from the ice accreting airfoil surface became much more obvious, the large-scale flow separation zone over the airfoil surface was found to become so big that almost cover the entire upper surface of the test model, as shown clearly in Fig. 6(e)–(f). It indicates that, the airflow over the test model, which was originally in an attached flow regime, as shown clearly in Fig. 6(a), would become in airfoil stall state, due to the significant ice accretion over the airfoil surface. The formation and expansion of the large-scale flow separation zone over the airfoil surface as induced by the ice

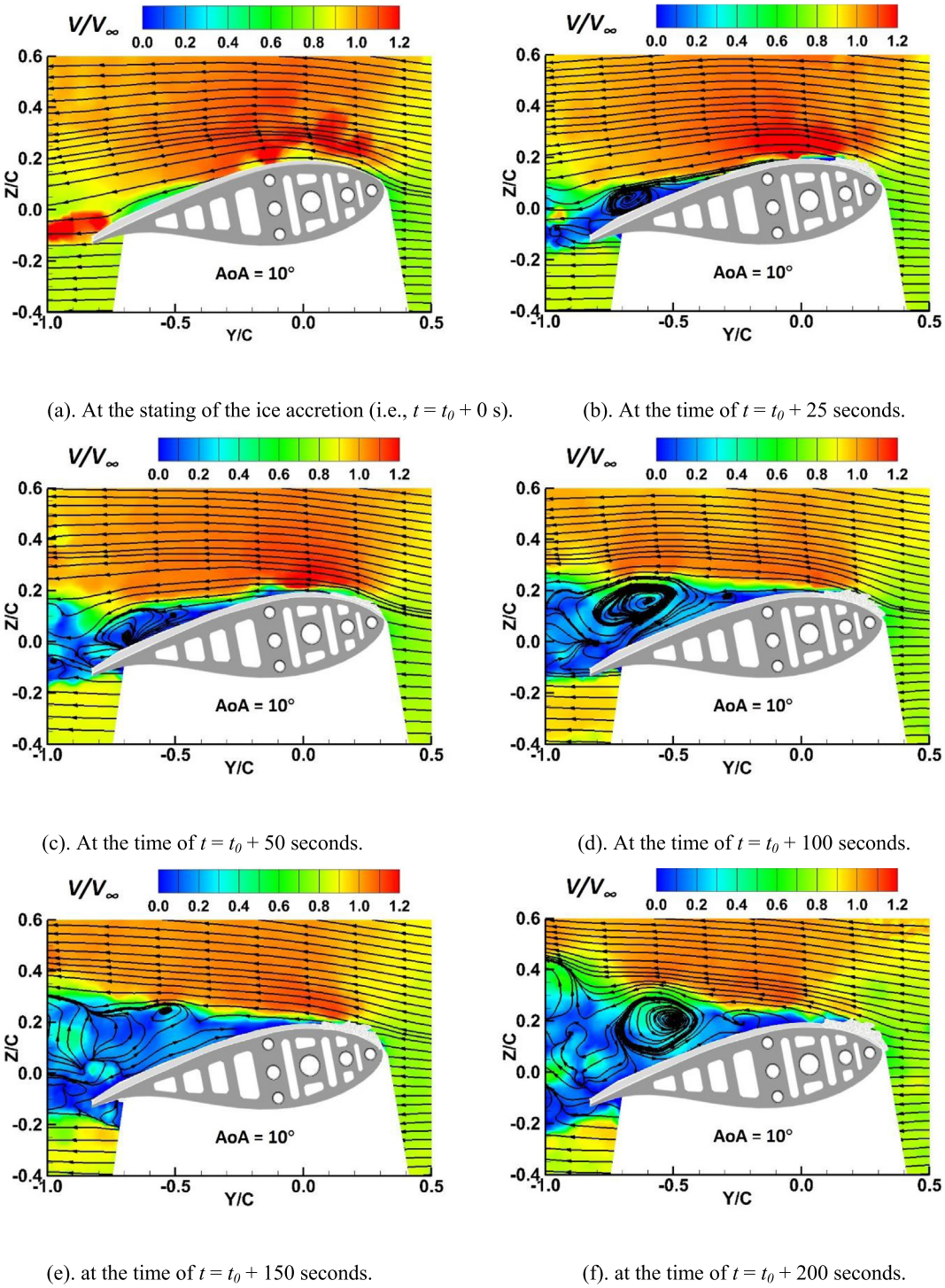

Fig. 6. Instantaneous PIV measurement results to reveal the dynamic changes of the airflow over the ice accreting surface of the turbine blade model as a function of the ice accretion time.

accretion would cause a dramatic degradation on aerodynamic performance of the turbine blade model (i.e., significant lift decreasing and rapid drag increasing), which was confirmed quantitatively from the aerodynamic force measurement results to be presented in next section.

In the presents study, PIV measurements were also used to reveal the significant changes of the ensemble-averaged airflow characteristics induced by the ice accretion over the test model at different angles of attack. Fig. 7 shows the ensemble-averaged flow velocity distributions over the test model before ice accretion experiment (i.e., the test case with "clean" test model) and "after" 200 s of the ice accretion process under the glaze icing condition of $V_\infty = 40.0$ m/s, $T_\infty = -5.0\,^\circ$C, and LWC $= 1.1$ g/m^3 with the test model at AoA $= 5^\circ$, 10°, and 15°, respectively. It can be seen clearly that, for the test cases with the angle of attack being relatively small, i.e., smaller than the airfoil stall angle of AoA $\approx 11^\circ$ as

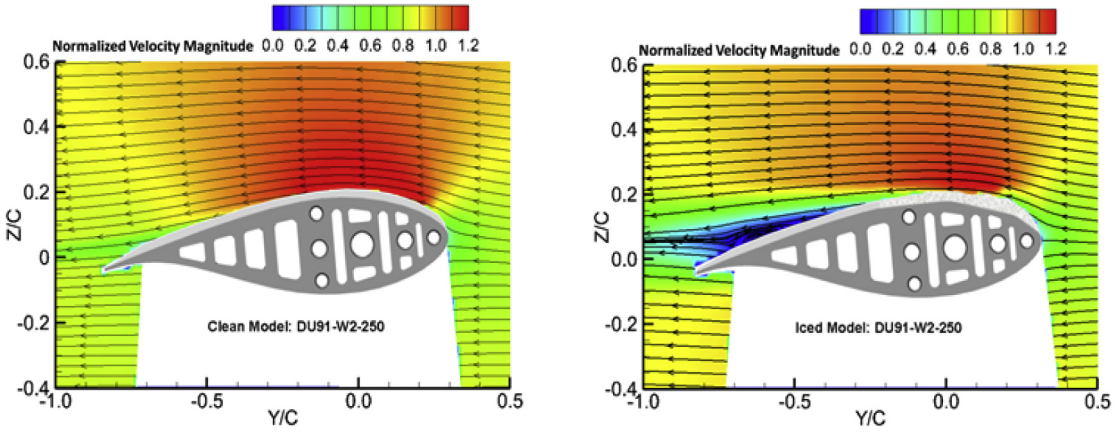

(a). The "clean" test model at AoA = 5 °.

(b). The "iced" test model at AoA = 5 °.

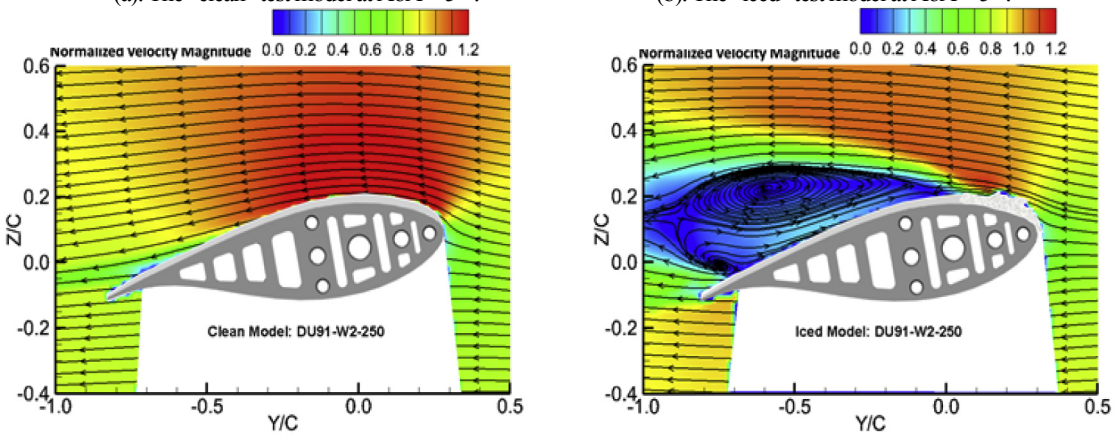

(c). The "clean" test model at AoA = 10 °.

(d). The "iced" test model at AoA = 10 °.

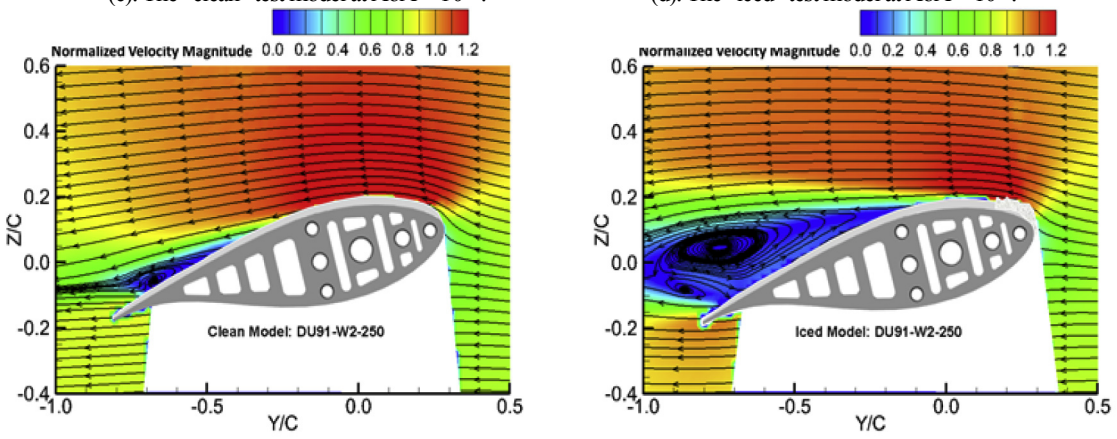

(e). The "clean" test model at AoA = 15 °.

(f). The "iced" test model at AoA = 15 °.

Fig. 7. Comparisons of the flow fields around the test model before ice accretion and after 200 s of ice accretion at different angles of attack.

revealed in Fig. 2, the incoming airflow was found to be quite compliant as flowing over the test model, i.e., the streams of the incoming airflow would flow smoothly along with streamlined profile of the "clean" airfoil model, as shown clearly in Fig. 7(a) and (c). Since significant amounts of irregular-shaped ice structures were found to accrete over the airfoil surface after 200 s of the ice accretion experiment, as shown in Figs. 4 and 5, the ice accretion would disturb the development of the boundary layer airflow over the airfoil surface greatly. As a result, the incoming airflow was found to separate from the airfoil upper surface at the downstream location of ~50% chord length for the test case of AoA = 5°, resulting in a large-scale flow separation zone over the upper surface of the

test model, covering almost half of the airfoil surface, as shown clearly in Fig. 7(b). For the test case of AoA = 10°, due to the existence of the irregular-shaped ice structures accreted around the airfoil leading edge, the incoming airflow were found to be detached from the airfoil surface at an upstream location near the airfoil leading edge, resulting in a very large flow separation zone covering almost entire upper surface of the test model, as shown clearly in Fig. 7(d). Formation of such a big flow separation zone over the upper surface of the test model is suggested to be responsible for the dramatic lift decrease and drag increase for the iced airfoil model revealed from the aerodynamic force measurements to be discussed in next section.

As the angle of attack of the test model was further increased to AoA = 15°, since it is beyond the stall angle for the "clean" airfoil model, an evident flow separation zone was observed near the trailing edge of the "clean" airfoil model, as shown clearly in Fig. 7(e). As shown in Figs. 4 and 5, with the test model being at the relatively high angles of attack AoA = 15°, ice structures were found to accrete mainly on the pressure-side (i.e., lower surface) of the test model, and only a small amount of ice would accrete on the airfoil upper surface. As a result, as shown in Fig. 7(f), even though the flow separation zone siting over the upper surface of the "iced" test model was found to enlarge substantially in comparison to that of the "clean" test model case, the size and the covering range of the flow separation zone were found to be smaller than those of the AoA = 10° case. It indicates that, the aerodynamic performance degradation of the test model induced by ice accretion could be more significant for the test cases with relatively smaller angles of attack, which were verified more quantitatively based on the aerodynamic force measurements to be presented in next section.

3.4. Aerodynamic force measurements of the test model during the ice accreting process

As described above, the aerodynamic forces (i.e., lift and drag) acting on the turbine blade model were also measured during the ice accreting process by using two sets of high-sensitive, multi-axis force-moment transducers (i.e., ATI-IA Mini 45) mounted at the two ends of the test model. Fig. 8 shows the time evolutions of the instantaneous measurement results of the aerodynamic forces (i.e., in terms of lift and drag coefficients) during the dynamic ice accretion process with the test model being set at AoA = 5°, 10°, and 15°, respectively. While the instantaneous aerodynamic forces (i.e., lift and drag) acting on the test model were measured at a data acquisition rate of 350 Hz, the moving-averaged results were also given in the plot, which were obtained by averaging the instantaneous force measurement data over every 2.0 s in duration. Corresponding to the aerodynamic force measurements, the acquired snapshot images of the dynamic ice accreting process and the PIV measurements of the airflow over the surface of the turbine blade model were described above and shown in Figs. 4–7.

As shown clearly in Fig. 8(a), with the test model being at a relatively small angle of attack, i.e., at AoA = 5°, while the lift coefficient of the turbine blade mode was found to be approximately $C_L = 1.0$ before starting the ice accretion process, the corresponding drag coefficient is relatively small, i.e., $C_D = 0.05$. Upon switching on the water spray system of the ISU-IRT at the time instance of $t = t_0$, the airborne super-cooled water droplets would impinge onto the surface of the test model to start the ice accretion process over the airfoil surface immediately. As aforementioned, the ice structures were found to accrete not only within the direct impingement zone near the airfoil leading edge, but also at further downstream locations over the airfoil surface due to the surface water runback under such a glaze icing condition. As a result, the lift force acting on the test model was found to decrease rapidly, while the drag force increases monotonically, as the time increases. It can also be seen that, after about 100 s of the ice accretion experiment, the decreasing rate of lift force was found to become more moderate, while the fluctuation amplitudes of the instantaneous aerodynamic forces acting on the test model were found to increase gradually, as indicated by the much wider fluctuating margins of the instantaneous lift and drag data given in Fig. 8(a). The rapid decrease of the lift force in the early stage of the icing process, i.e., $t \leq 100$ s, was believed to be caused by the formation of the initial ice roughness and fast runback of the surface water to form irregular-shaped ice features over the airfoil surface at the beginning of the ice accretion process. Since the irregular-shaped ice structures accreted over the airfoil surface would dramatically change the streamlined profile of the test model, the streamlines of the incoming airflow were found to separate from the airfoil surface, resulting in the formation of large-scale flow separation zone over the surface of the test model, as revealed clearly from the PIV measurement results described above. After a certain time of the ice accretion process, e.g., $t > 100$ s for this test case of AoA = 5°, most of the front surface of the test model (i.e., the region near the airfoil leading edge) was found to be covered by accreted ice layer, as shown clearly in Figs. 4 and 5. As the ice accretion process continues, while the ice layer accreted around the airfoil leading edge became thicker and thicker and extruded further outward into the incoming airflow, the degradation of the aerodynamic performance (i.e., the lift reduction and drag increase) at the later stage of the ice accretion process was mainly caused by the continuously increasing of the large-scale flow separation over the airfoil surface induced by thicker and thicker ice layer accreted around the airfoil leading edge. The larger fluctuating amplitudes of the instantaneous aerodynamic forces (i.e., both lift and drag) acting on the test model in the later stage of the ice accretion process are believed to be closely related to the generation and shedding of unsteady vortex structures induced by the irregular-shaped ice structures accreted over the airfoil surface, as revealed clearly from the instantaneous PIV measurement results given in Fig. 6.

As the angle of attack of the airfoil model increases to AoA = 10°, the evolution characteristics of the measured lift and drag profiles were found to be very similar to those described above for the test case of AoA = 5°. As shown clearly in Fig. 8(b), the early stage of ice accretion process with rapid lift decreasing rate was found to end at $t \approx 150$ s, when the decreasing rate of the lift was found to slow down slightly for this test case. As the ice accretion process continues, corresponding to the more complex airflow characteristics (i.e., flow separation and shedding of unsteady vortex structures) induced by the ice accretion over the airfoil surface, the fluctuating amplitudes of the instantaneous aerodynamic forces acting on the test model were found to increase substantially, in comparison with those of the test case of AoA = 5°. With more and more ice structures accreted over the turbine blade model, the drag force acting on the test model was found to increase almost linearly with the ice accretion time, as shown in Fig. 8(b).

When the angle of attack of the test model was further increased to 15° (i.e. AoA = 15°), even for the "clean" test model would be in a stall state for this test case, as shown in Fig. 3. A large-scale flow separation zone would be formed over the upper surface of the test model even before the icing experiment started. As shown clearly in Figs. 4 and 5, while the ice accretion would be mainly occurred on the pressure side (i.e., lower surface) of the airfoil model, only a small amount of ice would accrete near the airfoil leading edge on the suction side (i.e., upper surface) of the airfoil surface, which would enlarge the flow separation over the upper surface of the test model slightly. As a result, no sharp decrease of the lift was found for this case in the beginning of ice accretion process. Instead, a gradual lift degradation was observed throughout the entire ice

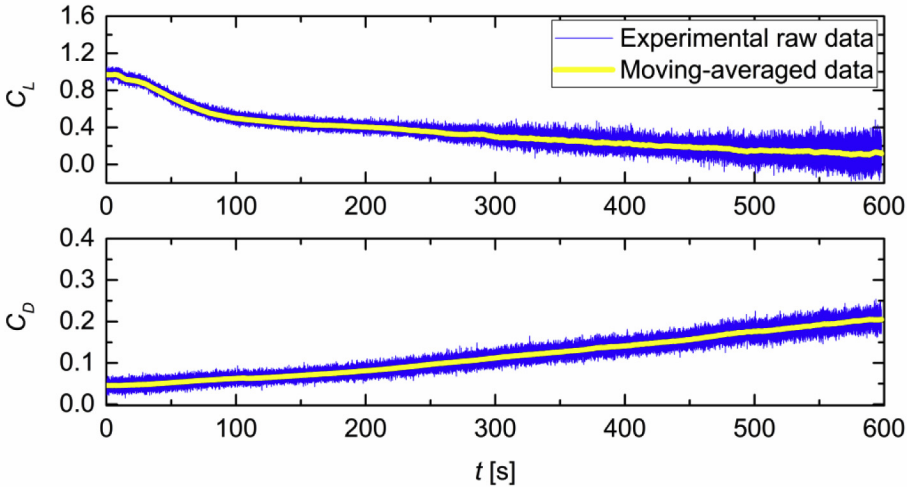

(a). At AoA = 5 °.

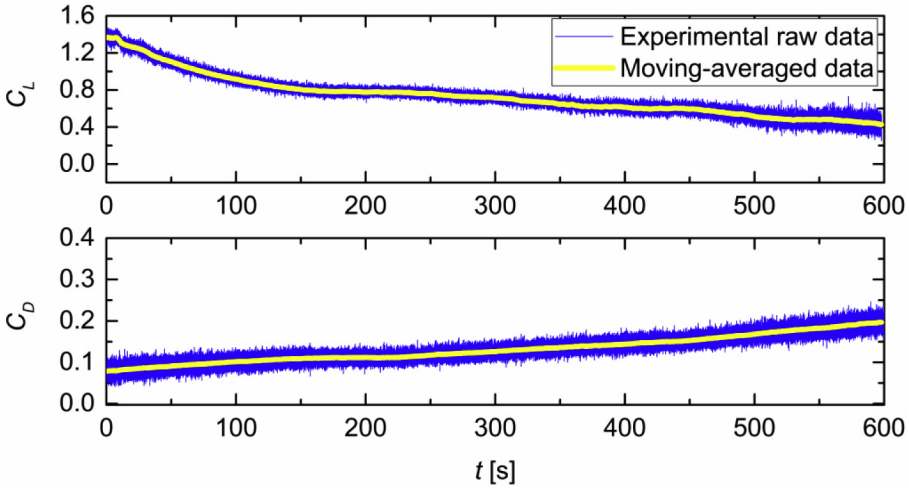

(b). At AoA = 10 °.

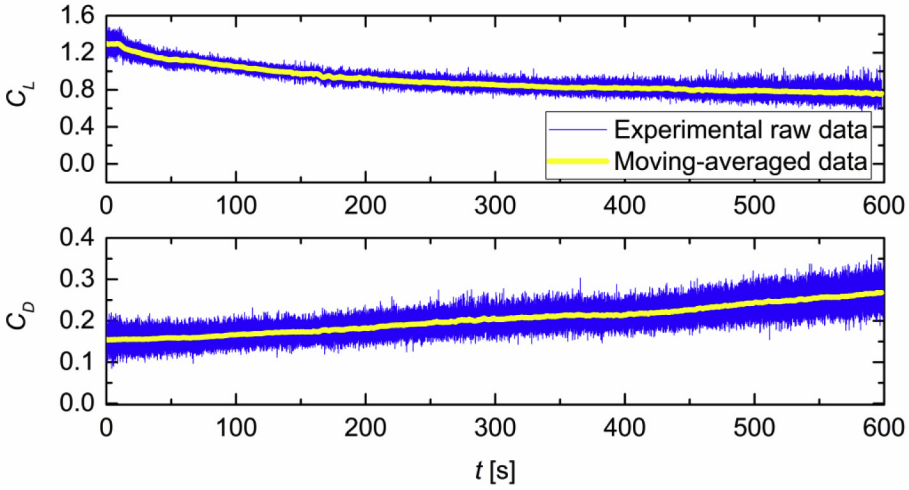

(c). At AoA = 15 °.

Fig. 8. Measured lift and drag coefficients of the test model during the dynamic ice accreting process at different angles of attack.

accretion process, as shown in Fig. 8(c). This observation is quite different from those of the test cases with relatively lower angles of attack (i.e., lift was found decrease rapidly at the initial stage of the icing process, and then turn to a much moderate decreasing rate at later time of the ice accretion process). It can also be seen clearly that, the drag coefficient of the ice accreting airfoil was still found to increase almost linearly with the time for this test case as well, corresponding to the increasing friction and growing of the flow separation zone during the ice accretion process.

Fig. 9 gives the normalized lift and drag coefficients of the test model (i.e., normalized by the corresponding values before starting the ice accretion experiment) as a function of the ice accretion time with the test model at different angles of attack, which can be used to reveal the effects of ice accretion process on the aerodynamic performance degradation of test model more clearly and quantitatively. It can be seen clearly that, the degradation rate of the aerodynamic performance of the turbine blade model induced by the dynamic ice accretion process would change significantly at different angles of attack. For the same turbine blade model, ice accretion would degrade the aerodynamic performance of the test model (i.e., in terms of lift increasing and drag increasing) much more significantly at smaller angles of attack. More specifically, as shown in Fig. 9(a), while the lift force acting on the test model was found to become only 12% of its original value (i.e., before starting the ice accretion experiment) after 600 s of the ice accretion experiment for the test case of AoA = 5°, the responding values for the AoA = 10° and AoA = 15° cases were found to be 31% and 59%, respectively. As described above, when the angle of attack of the test model is relatively small, more irregular-shaped ice structures were found to accrete over the suction side (i.e., upper surface) of the test model. The irregular-shaped ice structures would dramatically change the characteristics of the airflow over the surface of the test model, resulting in a more significant lift reduction for the test cases with relatively smaller angles of attack. Meanwhile, the ice accretion over the surface of the test model would also greatly increase the friction drag as well as the pressure drag associated with the formation of the large-scale flow separation zone over the airfoil surface. Therefore, as shown clearly in Fig. 9(b), the normalized drag acting on the ice accreting airfoil model was found to increase much more rapidly for the test cases with relatively smaller angles of attack. After 600 s of the ice accretion experiment, the drag force acting on the test model was found to increase by about 4.5 times for the test case with AoA = 5°, while the drag forces for the AoA = 10° and AoA = 15° cases were found to increase by 2.5 times and 1.7 times, respectively.

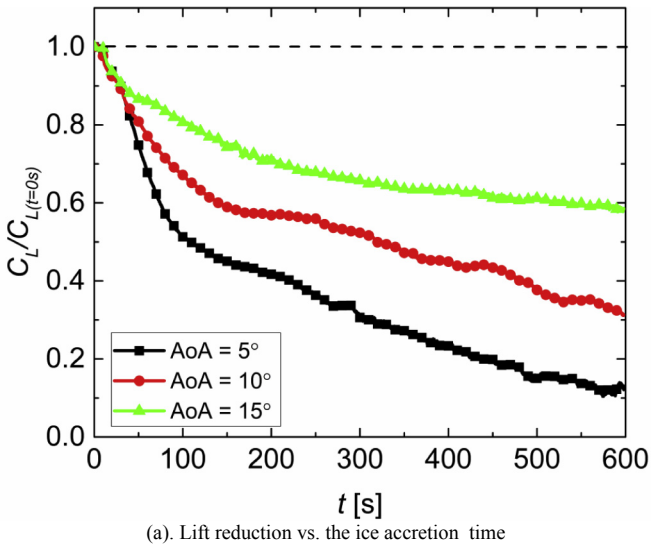

(a). Lift reduction vs. the ice accretion time

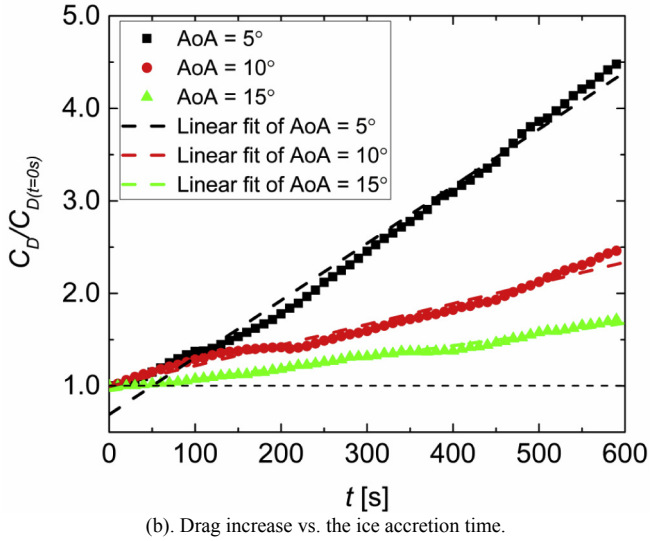

(b). Drag increase vs. the ice accretion time.

Fig. 9. Aerodynamic performance degradation of the test model induced by the ice accretion at different angels of attack.

4. Conclusions

In the present study, a comprehensive experimental investigation was conducted to characterize the dynamic ice accretion process over the surfaces of wind turbine blades and evaluate its effects on the aerodynamic performance degradation of the turbine blades. The experimental study was performed in an Icing Research Tunnel available at Iowa State University (i.e., ISU-IRT). A polymer-based, turbine blade section model with a DU91-W2-250 airfoil shape in the cross section was manufactured and used for the ice accretion experiment. While a high-resolution imaging system was used to record the dynamic ice accretion process over the airfoil surface, the aerodynamic forces acting on the test model during the dynamic ice accretion process were measured by using two sets of high-sensitive multi-axis force/moment systems mounted at two ends of the turbine blade model. In addition, a high-resolution digital Particle Image Velocimetry (PIV) system was also used to characterize the turbulent airflow over the ice accreting surface of the test model. The detailed airflow field measurements were correlated with the aerodynamic force data to elucidate the underlying physics pertinent to the significant degradation in the aerodynamic performance of the wind turbine blades induced by the dynamic ice accretion process.

The ice accretion experiment was performed under a typical glaze icing condition of $V_\infty = 40.0$ m/s, $T_\infty = -5.0$ °C, and LWC = 1.1 g/m^3. Upon the impingement of airborne super-cooled water droplets onto the airfoil surface, ice was found to accrete rapidly the surface of the test model. Due to the insufficient heat transfer to remove/dissipate all the released latent heat of fusion associated with the solidification process of the super-cooled water droplets, only a portion of the impacted super-cooled water droplets were found to turn into ice upon impact, and the rest of the impacted water mass remained in liquid state and ran back rapidly as driven by the boundary layer airflow over the airfoil surface. The runback surface water was found to be frozen eventually at further downstream locations, resulting in the formation of complicated rivulet-shaped ice structures in the region far beyond the direct impingement zone of the supercooled droplets. As the time goes by, the ice structures accreted over the airfoil surface were found to grow rapidly and extruded into the incoming airflow to capture

more supercooled water droplets to amplify the further growth of the ice structures. While ice was found to accrete over both the lower and upper surfaces of the test model, the ice accretion over the lower surface was found to be much severer than those over the upper surface. As the angle of attack increases, while more and more ice structures were found to accrete over the lower surface of the test model, ice accretion region over the upper surface of the test model was found to become less and less.

The PIV measurements revealed clearly that the streamlines of the incoming airflow would conform well to the smooth, streamlined airfoil profile of the turbine blade model before starting the ice accretion process. After starting the ice accretion process, due to the rapid ice accretion to form irregular-shaped ice roughness/structures over the airfoil surface, especially for those accreted near the airfoil leading edge, the streamlined profile shape of the test model was found to be deformed substantially. The development of the boundary layer airflow over the airfoil surface was found to be affected significantly. Induced by the ice accretion, the incoming airflow was found to separate from the ice accreting airfoil surface, causing the formation of a large-scale flow separation zone sitting over the upper surface of the test model. As the ice accretion time goes by, with the continuous growth of the complicated ice structures accreted over the test model, the separation point of the incoming airfoil was found to move further upstream, resulting in the continuous expansion of the large-scale flow separation zone over the airfoil surface during the dynamic ice accretion process. Meanwhile, more and more unsteady vortex structures were also found to be generated and shed from the ice accreting airfoil surface. The rapid expansion of the large-scale flow separation zone formed over the airfoil surface induced by the dynamic ice accretion was found to cause a dramatic degradation for the aerodynamic performance of the turbine blade model.

The aerodynamic force measurements confirmed quantitatively that, after irregular-shaped ice structures starting to accrete on the turbine blade model, while the lift of the model was found to decrease rapidly, the drag acting on the test model was found to increase significantly. While the drag force acting on the test model was found to increase almost linearly with the ice accretion time, the lift was found to decrease at a much greater rate at the initial icing stage (e.g., $t \leq 100$ s for AoA $= 5^\circ$ case, and $t \leq 150$ s for AoA $= 10^\circ$ case) than those at the later stage of the ice accretion process. The rapid lift degradation at the early stage of the ice accretion process was believed to be caused by the transition of the attached airflows to separate from the airfoil surface induced by the quick growth of ice roughness accreted over the airfoil surface at the beginning of the ice accretion process, as revealed clearly from the PIV measurements. After a certain time of the ice accretion process, the front surface of the test model (i.e., the regions near the airfoil leading edge) would be covered by a thick ice layer. The further degradation of the aerodynamic performance (i.e., the lift reduction and drag increase) at the later stage of the ice accretion process was mainly caused by the continuous expansion of the large-scale flow separation zone formed over the ice accreting airfoil surface. The fluctuating amplitudes of the aerodynamic forces (both lift and drag) acting on the test model were found to increase substantially at the later stage of the ice accretion process, which is believed to be closely related to the generation and shedding of more unsteady vortex structures induced by the more complex ice structures accreted over the airfoil surface at the later stage of the ice accretion process.

It was also found that, the aerodynamic performance degradation of the turbine blade model induced by ice accretion would be a strong function of the angle of attack of the test model. For the same turbine blade model, the aerodynamic performance degradation (i.e., in terms of lift increasing and drag increasing) induced by ice accretion was found to be much more significantly at relatively smaller angles of attack. More specifically, after 600 s of the ice accretion experiment, while the lift force acting on the test model was found to become only 12% of its original value (i.e., the value before starting the ice accretion process) for the AoA $= 5^\circ$ case, the corresponding values for the AoA $= 10^\circ$ and AoA $= 15^\circ$ cases were found to be about 31% and 59%, respectively. Meanwhile, the drag force was found to increase about 4.5 times due to the ice accretion for the test case with AoA $= 5^\circ$, while the drag forces were found to increase only about 2.5 times and 1.7 times for the test cases of AoA $= 10^\circ$ and AoA $= 15^\circ$, respectively.

It should be noted that, while several previous studies have been carried out recently to simulate ice accretion on turbine blades through icing wind tunnel testing or using “artificial” iced profiles with various types and amounts of ice accretion to investigate the aerodynamic performance of iced blades, the experimental work presented here is believed to be the first to examine the dynamic ice accretion process over the surface of turbine blade model and characterize the resultant aerodynamic performance degradation in the course of the ice accreting process. The new findings derived from the present studies would lead to a better understanding of underlying physics pertinent to the icing phenomena, which could be used to improve current ice accretion models for more accurate prediction of ice formation and ice accretion on wind turbine blades as well as to develop innovative anti-/de-icing strategies (e.g., active pitch control based strategy for wind turbine icing mitigation by leveraging the significant difference in the icing-induced performance degradation at different angles of attack) tailored for safer and more efficient operations of wind turbines in cold weathers.

Acknowledgments

This research is supported by National Science Foundation (NSF) under award numbers of CBET- 1064196 and CBET-1435590. The authors want to thank Dr. Rye Waldman of Iowa State University for his help in conducting the present study.

References

[1] T. Wallenius, V. Lehtomäki, Overview of cold climate wind energy: challenges, solutions, and future needs, Wiley Interdiscip. Rev. Energy Environ. 5 (2016) 128–135, https://doi.org/10.1002/wene.170.
[2] N. Dalili, A. Edrisy, R. Carriveau, A review of surface engineering issues critical to wind turbine performance, Renew. Sustain. Energy Rev. 13 (2009) 428–438, https://doi.org/10.1016/j.rser.2007.11.009.
[3] B. Tammelin, M. Cavaliere, H. Holttinen, C. Morgan, H. Seifert, K. Säntti, Wind Energy Production in Cold Climate (WECO), ETSU Contract, 1999, pp. 1–38. Rep. W/11/00452/REP, UK DTI, http://scholar.google.com/scholar?hl=en&btnG=Search&q=intitle:WIND+ENERGY+PRODUCTION+IN+COLD+CLIMATE+(+WECO+)#8.
[4] F. Lamraoui, G. Fortin, R. Benoit, J. Perron, C. Masson, Atmospheric icing impact on wind turbine production, Cold Reg. Sci. Technol. 100 (2014) 36–49, https://doi.org/10.1016/j.coldregions.2013.12.008.
[5] O. Parent, A. Ilinca, Anti-icing and de-icing techniques for wind turbines: critical review, Cold Reg. Sci. Technol. 65 (2011) 88–96, https://doi.org/10.1016/j.coldregions.2010.01.005.
[6] G. Fortin, J. Perron, Wind turbine Icing and de-icing, in: 47th AIAA Aerosp. Sci. Meet. Incl. New Horizons Forum Aerosp. Expo, 2009, pp. 1–23, https://doi.org/10.2514/6.2009-274.
[7] S. Barber, Y. Wang, Wind Energy, in: European Wind Energy Conference (EWEC 2010) the Impact of Ice Formation on Wind Turbine Performance and Aerodynamics Abstract, 2010.
[8] Y. Liu, H. Hu, An experimental investigation on the unsteady heat transfer process over an ice accreting airfoil surface, Int. J. Heat Mass Tran. 122 (2018) 707–718, https://doi.org/10.1016/j.ijheatmasstransfer.2018.02.023.
[9] Y. Liu, L. Li, H. Li, H. Hu, An experimental study of surface wettability effects on dynamic ice accretion process over an UAS propeller model, Aero. Sci. Technol. 73 (2018) 164–172, https://doi.org/10.1016/j.ast.2017.12.003.
[10] M. Vargas, J. Tsao, Observations on the growth of roughness elements into icing feathers, in: 45th AIAA Aerosp. Sci. Meet. Exhib., AIAA, 2007, 2007-0900.
[11] S. Campbell, A. Broeren, M. Bragg, D. Miller, Aircraft performance sensitivity to

icing cloud conditions, in: 45th AIAA Aerosp. Sci. Meet. Exhib., American Institute of Aeronautics and Astronautics, Reston, Virigina, 2007, https://doi.org/10.2514/6.2007-86.
[12] G. Fortin, J.L. Laforte, A. Ilinca, Heat and mass transfer during ice accretion on aircraft wings with an improved roughness model, Int. J. Therm. Sci. 45 (2006) 595–606, https://doi.org/10.1016/j.ijthermalsci.2005.07.006.
[13] M. Bragg, G. Gregorek, J. Lee, Airfoil aerodynamics in icing conditions, J. Aircraft 23 (1986) 76–81.
[14] C. Hochart, G. Fortin, J. Perron, A. Ilinca, Wind turbine performance under icing conditions, Wind Energy 11 (2008) 319–333, https://doi.org/10.1002/we.258.
[15] W.J. Jasinski, S.C. Noe, M.S. Selig, M.B. Bragg, Wind turbine performance under icing conditions, J. Sol. Energy Eng. 120 (1998) 60, https://doi.org/10.1115/1.2888048.
[16] Y. Liu, K. Zhang, H. Hu, An experimental investigation on the water runback process over an airfoil surface with realistic ice roughness, in: 8th AIAA Atmos. Sp. Environ. Conf., American Institute of Aeronautics and Astronautics, Reston, Virginia, 2016, https://doi.org/10.2514/6.2016-3140.
[17] Y. Liu, H. Hu, An experimental investigation on the convective heat transfer process over an ice roughened airfoil, in: 54th AIAA Aerosp. Sci. Meet., vol. 2, 2016, pp. 1–31, https://doi.org/10.2514/6.2016-1978.
[18] K. Zhang, T. Wei, H. Hu, An experimental investigation on the surface water transport process over an airfoil by using a digital image projection technique, Exp. Fluid 56 (2015) 1–16, https://doi.org/10.1007/s00348-015-2046-z.
[19] L. Gao, Y. Liu, H. Hu, An Experimental Study on Icing Physics for Wind Turbine Icing Mitigation, 2017, pp. 1–16, https://doi.org/10.2514/6.2017-0918.
[20] L. Gao, Y. Liu, H. Hu, An experimental investigation on the dynamic ice accretion process over the surface of a wind turbine blade model, in: 9th AIAA Atmos. Sp. Environ. Conf., 2017, pp. 1–18, https://doi.org/10.2514/6.2017-3582.
[21] W.A. Timmer, R.P.J.O.M. van Rooij, Summary of the Delft university wind turbine dedicated airfoils, J. Sol. Energy Eng. 125 (2003) 488, https://doi.org/10.1115/1.1626129.
[22] R.P.J.O.M. van Rooij, W.A. Timmer, Roughness sensitivity considerations for thick rotor blade airfoils, J. Sol. Energy Eng. 125 (2003) 468, https://doi.org/10.1115/1.1624614.
[23] J. Kiefer, M.A. Miller, M. Hultmark, M.O.L. Hansen, Effects of finite aspect ratio on wind turbine airfoil measurements, J. Phys. Conf. Ser. 753 (2016) 22040, https://doi.org/10.1088/1742-6596/753/2/022040.
[24] A.P, J.J. Harper, Low Speed Wind Tunnel Testing, third ed., Wiley & Sons, 1999.
[25] S. Nilanjan, Gap Size Effect on Low Reynolds Number Wind Tunnel Experiments, MS thesis, Virginia Tech, 1999.
[26] M.L. Blaylock, D.C. Maniaci, B. Resor, in: Numerical Simulations of Subscale Wind Turbine Rotor at Low Reynolds Number, 33rd Wind Energy Symposium, 2015, pp. 1–23, https://doi.org/10.2514/6.2015-0493.
[27] T.C. Yap, M.Z. Abdullah, Z. Husain, Z.M. Ripin, R. Ahmad, The Effect of turbulence intensity on the aerodynamic performance of airfoils, in: 4th Int. Conf. Mech. Eng., 2001, pp. 31–36.
[28] S. Wang, Y. Zhou, M.M. Alam, H. Yang, Turbulent intensity and Reynolds number effects on an airfoil at low Reynolds numbers, Phys. Fluids 26 (2014) 115107, https://doi.org/10.1063/1.4901969.
[29] R.M. Waldman, H. Hu, High-speed imaging to quantify transient ice accretion process over an airfoil, J. Aircraft 53 (2015) 369–377, https://doi.org/10.2514/1.C033367.
[30] M. Papadakis, G.W. Zumwalt, R. Elangonan, G.A.J. Freund, M. Breer, L. Whitmer, An Experimental Method for Measuring Water Droplet Impingement Efficiency on Two- and Three-dimensional Bodies, 1989.